Structural Characterization of the Li-Ion Battery Cathode Materials LiTi$_x$Mn$_{2-x}$O$_4$ (0.2 ≤ x ≤ 1.5): A Combined Experimental ^{7}Li NMR and First-Principles Study

Roberta Pigliapochi,[†] Ieuan D. Seymour,[†] Céline Merlet,[†,‡,§] Andrew J. Pell,[†,∥] Denissa T. Murphy,[⊥] Siegbert Schmid,[⊥] and Clare P. Grey*,[†]

[†]Department of Chemistry, University of Cambridge, Cambridge CB2 1EW, United Kingdom

[‡]CIRIMAT, Université Toulouse 3 Paul Sabatier, CNRS, INPT, Bât. CIRIMAT, 118, route de Narbonne, 31062 Toulouse cedex 9, France

[§]Réseau sur le Stockage Électrochimique de l'Énergie (RS2E), Fédération de Recherche CNRS 3459, 33 rue St. Leu, 80039 Amiens, France

[⊥]School of Chemistry, University of Sydney, Sydney, NSW 2006, Australia

Ⓢ *Supporting Information*

ABSTRACT: Titanium doping in lithium manganese oxide spinels was shown to be beneficial for the structural stability of the potential Li-ion battery cathode materials LiTi$_x$Mn$_{2-x}$O$_4$, 0.2 ≤ x ≤ 1.5, yet the distribution of Li/Ti/Mn in the structure and the cation oxidation states, both pivotal for the electrochemical performance of the material, are not fully understood. Our work investigates the changes in the local ordering of the ions throughout this series by using a combination of ^{7}Li NMR spectroscopy and ab initio density functional theory calculations. The ^{7}Li NMR shifts are first calculated for a variety of Li configurations with different numbers and arrangements of Mn ions in the first metal coordination shell and then decomposed into Li−O−Mn bond pathway contributions to the shift. These Li−O−Mn bond pathways are then used to simulate and assign the experimental NMR spectra of different configurations and stoichiometries beyond those in the initial subset of configurations via a random distribution model and a reverse Monte Carlo approach. This methodology enables a detailed understanding of the experimental ^{7}Li NMR spectra, allowing the variations in the local ordering of the ions in the structure to be identified. A random distribution of Ti^{4+}−Mn$^{3+/4+}$ sites is found at low Ti content (x = 0.2); an inhomogeneous lattice of Mn^{4+}-rich and Ti^{4+}-rich domains is identified for x = 0.4, and single-phase solid solution is observed for x = 0.6 and 0.8. A mixed Li−Mn^{2+} tetrahedral and Li−Mn$^{3+/4+}$−Ti octahedral configuration is determined for the x = 1.0 case. A specific cation ordering in the partially inverse LiTi$_{1.5}$Mn$_{0.5}$O$_4$ case is found, which transforms into a two-phase network of disordered Mn^{3+}-rich and ordered Mn^{2+}-rich domains for x = 1.1−1.4.
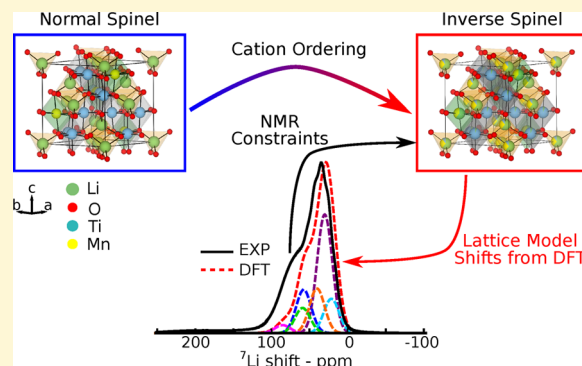
INTRODUCTION

Spinel-type lithium metal oxides are interesting cathode materials for rechargeable Li-ion battery applications. The robust host structure of spinel oxides retains capacity for many cycles, and the three-dimensional network of interstitial sites allows high Li diffusion rates.[1,2] LiMn$_2$O$_4$ spinel has been studied as a potential alternative to the more widely used LiCoO$_2$ because of its lower cost, lower toxicity, and higher thermal stability.[2,3] However, the application of Li$_x$Mn$_2$O$_4$ as a positive electrode is limited by the presence of Jahn−Teller active Mn^{3+} ions, which accelerate structural degradation of the material upon cycling due to a cooperative Jahn−Teller distortion.[4] Moreover, the charge disproportionation of 2Mn^{3+} → Mn^{4+} + Mn^{2+} results in the formation of Mn^{2+} ions, which dissolve in the electrolyte at the surface of the particles and deplete the spinel framework of transition-metal ions.[5] The electrochemical properties and the structural stability of LiMn$_2$O$_4$ were shown to be improved by introducing excess Li in the spinel structure to form Li$_{1+a}$Mn$_{2-a}$O$_4$.[6−9] The inclusion of the excess lithium raises the average Mn oxidation state, thereby reducing the amount of Jahn−Teller active Mn^{3+} ions. Another approach to limit the negative effects of the cooperative Jahn−Teller distortion has been to partially substitute the Mn ion with other transition metals (TM) such as Ni, Zn, and Ti, hence stabilizing the structural integrity of the electrode upon cycling.[10−13] Under-
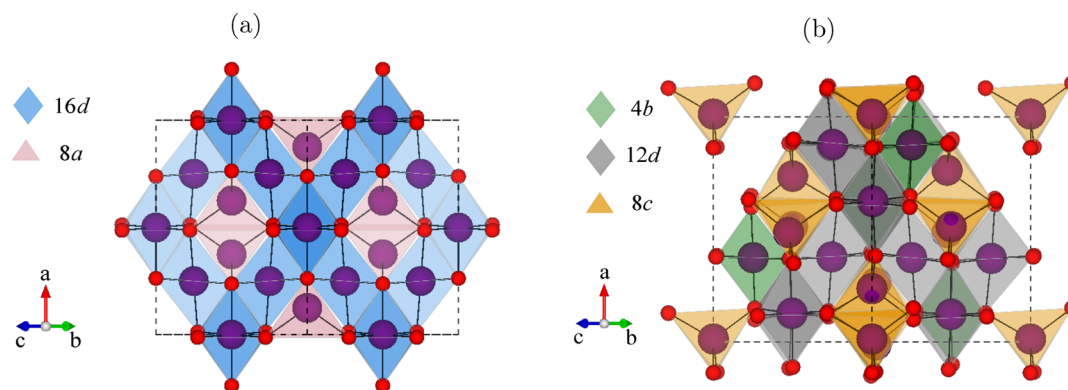
Figure 1. Polyhedral representation of a general spinel-type AB_2O_4 in the $Fd\bar{3}m$ (a) and $P4_332$ (b) space group with the A and B cations shown in purple spheres and the oxygens shown in red spheres. The crystallographically independent octahedral and tetrahedral sites are represented by polyhedra of different colors as labeled.

standing the structural ordering and the distribution of Li/TM ions in the structure is central to rationalizing the relationship between the electrochemical performance and the physical properties of the material. As an example, the kinetic and electrochemical properties of the high-energy $LiNi_xMn_{2-x}O_4$ cathode material have been analyzed in relation to the complex cation ordering throughout the series, unraveling the key role of compositional (dis)order in the electrochemical performance of this material.[14] Here, the randomization of Ni/Mn ions among the octahedral sites of the spinel lattice was proposed to lead to improved electrochemical performance.

In this work, we focus on the series of materials $LiTi_xMn_{2-x}O_4$ with $0.2 \leq x \leq 1.5$ and study the structural changes of the Mn-oxide spinel framework as an effect of Ti doping. In spinel materials of general formula AB_2O_4, the oxygen anions form a face-centered-cubic sublattice, within which octahedral (Oh) and tetrahedral (Td) interstitial sites are present in a 2:1 ratio. In a normal spinel, the A cations occupy the Td sites, and the B cations occupy the Oh sites (denoted as $A[B_2]O_4$), while in an inverse spinel, the B cations occupy all of the Td sites and half of the Oh sites, and the A cations occupy the other half of the Oh sites (denoted as $B[AB]O_4$). In the case of $LiTi_xMn_{2-x}O_4$, the partial substitution of Mn with Ti results in a mixed cation occupancy on both the Oh and Td sites of the spinel lattice.[15,16] In the $LiTi_xMn_{2-x}O_4$ series for $0.2 \leq x \leq 1.0$, the disordered $Fd\bar{3}m$ cubic spinel preferentially forms (Figure 1a) with proposed partial occupancy of Li^+/Mn^{2+} and $Li^+/Ti^{4+}/Mn^{3+/4+}$ on the tetrahedral 8a and the octahedral 16d sites, respectively, and with the Li(Oh)/Mn^{2+}(Td) fraction increasing with increasing Ti content. For $x > 1.0$, the more ordered $P4_332$ cubic spinel also starts to form (Figure 1b), in which it was proposed that the two inequivalent octahedral sites, 4b and 12d, are occupied by a mixture of $Li^+/Mn^{3+/4+}$ and a mixture of $Li^+/Ti^{4+}/Mn^{3+/4+}$ ions, respectively, while the tetrahedral 8c sites are partially occupied by Li^+/Mn^{2+} ions.[15,16] A detailed study using synchrotron X-ray, neutron powder diffraction, and XANES spectroscopy further investigated the effects of different sintering temperatures and cooling regimes during synthesis on the phase behavior of $LiTiMnO_4$.[17] Although it is a challenge to provide an accurate description of the coordination site disorder throughout the $LiTi_xMn_{2-x}O_4$ series because of the presence of multiple mixed-valence transition metals, a detailed characterization of the structure provides the fundamental basis with which to understand and monitor the electrochemical properties of the material. Analysis

based on X-ray diffraction (XRD) showed limited accuracy in determining the distribution of Li, Ti, and Mn ions in the lattice due to the difficulty of detecting Li in the presence of heavier elements and of distinguishing between Ti and Mn, which have similar X-ray scattering factors.[15,16] Electron spin resonance (ESR) studies were also used in combination with XRD analysis, but the presence of multiple Mn oxidation states made the assignment of the TM distribution challenging.[16]

$^{6/7}$Li NMR has been successfully used to characterize the local Li environments and the cation ordering in similar systems such as $LiMn_2O_4$,[18,19] $LiZn_xMn_{2-x}O_4$,[19−21] and $LiNi_xMn_{2-x}O_4$,[19,22] as well as in Li-excess Mn oxides, $Li_{1+a}Mn_{2-a}O_4$.[23,24] The dominant interaction leading to the observed $^{6/7}$Li NMR shift in this class of paramagnetic materials is the isotropic Fermi contact (FC) hyperfine interaction,[25−27] which results from the coupling between the nuclear moment of the Li and the time-average of the local field due to the unpaired d electrons present on the neighboring TM ions.[19,28] In the series of systems studied here, Ti is present as Ti^{4+} throughout (i.e., d^0 ion); hence, the only paramagnetic centers are the $Mn^{2+/3+/4+}$ sites (i.e., $d^5/d^4/d^3$ ions, respectively). The Fermi contact interaction is proportional to the unpaired spin density transferred from the d orbitals of Mn to the s orbitals of Li. This transfer can occur either directly through the overlap of the involved orbitals or, more prominently in the systems studied here, indirectly via the bridging oxygen p orbitals which form Mn−O−Li bond pathways. The observed ^{7}Li Fermi contact shift is hence given by the sum of the individual Mn−O−Li pathway contributions.[29] The sign and magnitude of the shift depend on the geometry and covalency of the pathway as well as on the Mn oxidation state and on the magnetic susceptibility of the material. In mixed cation systems, the variety of Li environments often results in a multitude of paramagnetic shifts and a significant broadening of the resonances, making the spectra difficult to interpret.[30] Computational predictions and ab initio calculations of paramagnetic NMR parameters constitute a robust and invaluable aid for the understanding of experimental NMR spectra of paramagnetic solids.

In this work, we report a detailed ^{7}Li magic-angle spinning (MAS) NMR spectroscopy investigation of the $LiTi_xMn_{2-x}O_4$ spinel series using state of the art spectroscopic methods for paramagnetic materials.[31] The interpretation of the experimental spectra is supported by first-principles density functional theory (DFT) calculations of the magnetic interactions

and ^{7}Li NMR shifts. Different LiTi$_x$Mn$_{2-x}$O$_4$ structures of (possibly fictitious) ferromagnetically aligned TM ions are simulated, from which we calculate the Mn−O−Li bond pathway contributions to the ^{7}Li hyperfine shift of the various environments, nominally at 0 K.[29] To compare these shifts with the experimental spectra obtained at finite temperature, we evaluate the possible Mn−Mn magnetic interactions, determine the Curie−Weiss magnetic factors, and use these to scale the shifts obtained with density functional theory (DFT) to the paramagnetic regime of the NMR experiments (performed at room temperature).[32,33] The library of bond pathway contributions are subsequently used to simulate the spectra of different LiTi$_x$Mn$_{2-x}$O$_4$ configurations in a combined random distribution model and reverse Monte Carlo approach, allowing the characterization of the cation ordering throughout the series. A random distribution of Ti^{4+}−Mn$^{3+/4+}$ sites among the octahedral 16d environments ($Fd\bar{3}m$) is found at low Ti content (x = 0.2), which transforms into a lattice of Mn^{4+}-rich and Mn^{3+}-rich phases for x = 0.4 and a single-phase solid solution for x = 0.6 and 0.8. A partially inverse spinel configuration is identified for x = 1.0 with mixed Li−Mn^{2+} tetrahedral sites and mixed Li−Mn$^{3+/4+}$−Ti octahedral sites. A specific ion distribution is identified for the LiTi$_{1.5}$Mn$_{0.5}$O$_4$ case, involving ordering between the tetrahedral 8c and the octahedral 4b and 12d sites in the $P4_332$ lattice, corresponding to $(\text{Li}_{0.6}\text{Ti}_{0.1}\text{Mn}_{0.3})_{8c}[(\text{Li}_{0.4}\text{Mn}_{0.2})_{4b}(\text{Ti}_{1.4})_{12d}]\text{O}_4$. This further transforms into a network of Mn^{3+}-rich disordered $Fd\bar{3}m$ and Mn^{2+}-rich ordered $P4_332$ domains for the x = 1.1−1.4 series.

■ EXPERIMENTAL METHODS

Synthesis of LiTi$_x$Mn$_{2-x}$O$_4$ (0.2 ≤ x ≤ 1.5). LiTi$_x$Mn$_{2-x}$O$_4$ samples (x = 0.2, 0.4, 0.6, 0.8, 1.0, 1.1, 1.2, 1.3, 1.4, and 1.5) were prepared via the solid-state synthesis method presented in detail in ref 17. Details of the synthetic procedure are described in the Supporting Information. Table S1 in the Supporting Information summarizes the crystal data and cation compositions of the LiTi$_x$Mn$_{2-x}$O$_4$ series (x = 0.2, 0.4, 0.6, 0.8, 1.0, 1.2, 1.3, 1.5) reported in previous XRD studies.[16]

Solid-State MAS ^{7}Li NMR. Solid-state NMR spectra of the LiTi$_x$Mn$_{2-x}$O$_4$ samples (0.2 ≤ x ≤ 1.5) were acquired on a Bruker 200 Avance III spectrometer using a 1.3 mm probe with a MAS frequency of 60 kHz. The one-dimensional ^{7}Li spectra were recorded using a double-adiabatic spin−echo sequence,[31] employing a pair of 50 μs tanh/tan short high-powered adiabatic pulses (SHAPs) of 5 MHz sweep width[34,35] and a 1.025 μs 90° excitation pulse. All pulses used a radiofrequency (RF) field strength of 244 kHz. For each spectrum, 32 768 scans were acquired using a recycle delay of 30 ms. The experimental ^{7}Li NMR spectra were fitted using the DMFIT software.[36] An initial model was set up with components based on the hyperfine shifts predicted with DFT calculations, and the fitting of the isotropic region and the sideband pattern was then obtained by optimizing the shift and the amplitude of the deconvoluting regions.

■ COMPUTATIONAL METHODS

Formation Energies and Thermodynamical Phase Stability. *Methodology of Thermodynamical Phase Stability Analysis.* The thermodynamical phase stability of the LiTi$_x$Mn$_{2-x}$O$_4$ series was studied by calculating the formation enthalpy of various structures with different stoichiometries. For LiTi$_2$O$_4$ and LiMn$_2$O$_4$, crystal structures were obtained from the International Crystal Structure Database (ICSD) and fully relaxed (i.e., both the unit cell parameters and the atomic positions were allowed to vary) using DFT. From the LiTi$_2$O$_4$ and LiMn$_2$O$_4$ unrelaxed crystal structures, selected intermediate stoichiometries of the LiTi$_x$Mn$_{2-x}$O$_4$ series were generated using the Site Occupancy Disorder (SOD)[37] and the Cluster-Assisted Statistical Mechanics (CASM)[38,39] softwares. Specifically, for x = 0.5, 1.0, and 1.5, small cells of 14 atoms were considered, where all possible swaps

between Li, Ti, and Mn were enumerated. For the x = 1.25 and 1.5 cases, additional configurations were considered: for larger cells of 56 atoms, all configurations were enumerated starting from LiTi$_2$O$_4$ and replacing (2−x) Ti ions with Mn ions. Additionally, swaps between Li, Mn, and Ti were allowed to include inverse spinel lattices in the analysis, i.e. networks of mixed Ti−Mn−Li occupancy on both the tetrahedral and the octahedral sites were generated.

Details of GGA+U Calculations of Formation Energies. The unit cell parameters and atomic positions of each generated configuration were relaxed with DFT using the PBE[40] spin-polarized generalized gradient approximation (GGA) functional within the VASP code.[41] The projector augmented waves (PAW)[42] method was used with a plane-wave cutoff of 500 eV and an energy tolerance of 10^{-6} eV, resulting in a convergence of the energy of approximately 4 meV/atom. A force tolerance of 10^{-5} eV/Å was used for ionic relaxations, resulting in a convergence of the energy of approximately 4 meV/atom. A force tolerance of 10^{-5} eV/ \AA was used for ionic relaxations. The electronic energy of each relaxed structure was calculated with a single-point energy minimization. The reciprocal space sampling was performed with a k-point grid of 8 × 8 × 8 points for the smaller cells (14 atoms) and 4 × 4 × 4 points for the larger cells (56 atoms). To correct for the self-interaction error in the GGA formalism, a Hubbard U parameter was included for the Mn ions to treat the 3d correlations.[43] In this work, the approach proposed by Liechtenstein was used,[44] where the Coulomb matrix (U) and the exchange matrix (J) are combined to give an overall effective value U_{eff} = U − J. The value of J was fixed to 1 eV throughout. In a previous study by Wang et al.,[45] values of U_{eff} = 4.5, 4.0, and 3.5 eV were calculated for Mn^{2+}, Mn^{3+}, and Mn^{4+} ions, respectively. Because in our systems the Mn ions are present in multiple oxidation states, an average U_{eff} value of 3.9 eV was chosen for all the Mn sites.

Paramagnetic Shift Calculations. The calculation of the Fermi contact shift, δ_{FC}, adopted in this work follows the methodology presented by Kim et al.,[46] which is summarized here. In this method, the hyperfine coupling constant, A_{iso}, is first calculated from the system in the ferromagnetic state nominally at 0 K and then scaled using a Curie−Weiss factor, Φ, to match the paramagnetic regime typical of NMR experiments.

$$\delta_{\text{FC}} = \frac{A_{\text{iso}}10^6\Phi}{2h\nu} \quad (1)$$

with

$$A_{\text{iso}} = \frac{2}{3}\mu_0\mu_B\mu_N g_e g_I |\psi_N^{\alpha-\beta}|^2 \quad (2)$$

and

$$\Phi = \frac{B_0\mu_{\text{eff}}^2}{3k_B g_e\mu_B S(T-\theta)} \quad (3)$$

where h is the Planck constant, ν is the Larmor frequency, $|\psi_N^{\alpha-\beta}|^2$ is the unpaired spin density at the Li nuclear position, B_0 is the static magnetic field, μ_{eff} is the effective electronic magnetic moment, μ_B is the Bohr magneton, S is the formal electronic spin of the paramagnetic center(s), k_B is the Boltzmann constant, g_e is the free-electron g-value, g_I is the nuclear g-factor, T is the temperature used in the experiments, here estimated to be 320 K to account for frictional heating due to MAS NMR, and θ is the Weiss constant. In this work, μ_{eff} is taken to be the spin-only value of $2\mu_B\sqrt{S(S+1)}$. This is considered a good approximation for the class of systems studied here. As an example, in the case of LiMn$_2$O$_4$ with an average oxidation state of Mn$^{3.5+}$, S = 1.75, and the calculated spin-only value is μ_{eff} = 4.39 μ_B, in good agreement with the experimental μ_{eff} range of 4.33−4.36 μ_B reported by Masquelier et al.[47]

Methodology for Calculating the Magnetic Parameters θ and Φ. Values of θ were obtained ab initio by calculating the magnetic exchange coupling constants, J, by a multivariate linear regression of the DFT-calculated energies of systems with different magnetic configurations of coupled spins. More details of the method are

presented in the Supporting Information. The calculations of the various exchange coupling constants were performed on selected structures, i.e., the lowest energy configurations for the $LiTi_{0.5}Mn_{1.5}O_4$, $LiTiMnO_4$, $LiTi_{1.25}Mn_{0.75}O_4$, and $LiTi_{1.5}Mn_{0.5}O_4$ stoichiometries, containing networks of $Mn^{3+/4+}$, Mn^{3+}, $Mn^{2+/3+}$, and Mn^{2+} ions, respectively. When equivalent Mn–Mn interactions are present in different lattices, the corresponding J values were found to differ by less than 3%, differences arising from local distortions of the optimized geometries. All of the considered structures containing Mn^{3+} ions were found to exhibit a cooperative Jahn–Teller distortion.

Methodology of Hyperfine Coupling Constant, A_{iso}, Calculation. The isotropic value of the hyperfine tensor A_{iso}, in eq 2, was calculated with DFT by integrating the unpaired electron spin density, $|\psi_N^{\alpha-\beta}|^2$, directly at the Li nuclear position in the ferromagnetic state, which was then scaled to the paramagnetic regime by multiplying it by the scaling factor Φ (eq 1).[46] The bond pathway decomposition method presented by Middlemiss et al.[29] was followed to obtain the Mn–O–Li Fermi contact bond pathway contribution from each Mn ion to the total Li shift using the computed site-specific scaling factor, Φ_i.

Details of Hybrid DFT/Hartree–Fock Calculations of Paramagnetic Shifts. All calculations of magnetic and hyperfine parameters were performed in CRYSTAL09,[48] a solid-state DFT code using a Gaussian-type basis set to describe core states accurately. Because of the high dependence of the calculated paramagnetic shifts on the quality of the Gaussian basis sets, two types were utilized: a smaller basis set for geometry optimizations, and a more extended basis set for hyperfine and magnetic single-point calculations. More details are given in the Supporting Information. All calculations were performed with hybrid functionals in the spin polarized state. Previous ab initio studies on ^7Li paramagnetic NMR shifts show that values obtained using 20 and 35% Hartree–Fock (HF) exchange provide the upper and lower bounds for the experimental shifts.[29,30] Hence, separate calculations were performed with the B3LYP functional with 20% HF exchange[49] (denoted HYB20) and a modified B3LYP with 35% of HF exchange (denoted HYB35). The convergence of the energy and the spin density were checked with respect to the number of sampled points in the reciprocal space. The reciprocal space sampling was performed with a k-point grid of $4 \times 4 \times 4$ points in the simulated cells, which contain 56 atoms. Self-consistent field cycles were converged to an energy difference of 2.7×10^{-6} eV.

Simulation and Fitting of the ^7Li NMR Spectra. *Random Solution Model of a Single Phase.* To use the Fermi contact bond pathway contributions calculated from DFT to simulate model NMR spectra, one needs to know the possible cationic environments around the lithium ions and the population distribution among these environments. The simplest approximation that can be made to obtain such distributions of environments is to consider that there is no cation ordering, and thus, the cations are randomly distributed in the sites available to them. This approach corresponds to the random solid solution model. In the regular spinel structure, Li centers have the following neighboring cations: (1) each Li in a Td site has 12 neighbor cations located on Oh sites, which are each bound via an oxygen bridge and considered to contribute to the overall Fermi contact shift of this lithium; and (2) each Li in an Oh site has 12 neighbor cations, 6 of which are in Td sites and 6 of which are in Oh sites, which are each bound via an oxygen bridge and considered to give (different) contributions to the overall Fermi contact shift of this lithium. To simulate the NMR spectrum, we thus need to know (i) how the Li ions are distributed between Td and Oh sites and (ii) what ions are present in each Li neighboring shell. Once we know these possible configurations, we can calculate the corresponding Fermi contact shifts and estimate the probability of these environments to simulate the NMR spectrum. In the random solution model, for each Li environment with a given number of Mn and Ti neighbors, the number of all possible configurations is calculated with the corresponding probability p modulated by the stoichiometric ratio of the ions in the structure. For each environment, a Gaussian distribution is then generated of the form $G = p \cdot exp[-(\delta - \sum \delta_{path})^2/(2\omega^2)]$. In this formula, p is the probability associated with the environment considered, δ is the range of resonance values for which

the distribution is calculated, $\sum \delta_{path}$ is the sum of all relevant bond pathway contributions to the shift involved in the particular environment, and ω is the Gaussian width. An approximate Gaussian peak width of 15 ppm was used to model the individual environments based on previous NMR studies on $LiMn_2O_4$.[19] The simulated NMR spectrum is then obtained as the sum of the Gaussian plots corresponding to the various environments present in the system.

Reverse Monte Carlo Simulations of a Single Phase. While in some cases, the random solution model provides a good agreement with the experimental data, in other cases, such as the $LiTi_{1.5}Mn_{0.5}O_4$ material studied here, it does not, and there is a need to calculate the populations of lithium environments according to different conditions. Here, for this purpose, we use a simulation method inspired by reverse Monte Carlo approaches. The idea of a reverse Monte Carlo method is to build a large simulation box that is representative of the system under study and explore the effect of configurational changes. Starting from an initial configuration, i.e. a large number of ions with defined positions in space, we allow certain moves which are accepted or rejected depending on their agreement with chosen constraints.

In the present case, we built the large simulation box by replicating an initial spinel structure corresponding to $LiTi_{1.5}Mn_{0.5}O_4$ in the $P4_332$ space group. The initial structure contained 56 atoms corresponding to (i) 8 Li ions in Td sites ($8c$), (ii) 12 Ti ions and 4 Mn ions in Oh sites ($12d$ and $4b$, respectively), and (iii) 32 oxygen sites ($8c$ and $24e$). This simulation box was replicated 10 times in all 3 dimensions, leading to a large simulation box containing 8000 Li ions, 12 000 Ti ions, 4000 Mn ions, and 32 000 oxygen ions. We checked that this 10 × 10 × 10 system is large enough by simulating some of the NMR spectra with a larger box of 15 × 15 × 15 repeat units. The results from the two system sizes showed no significant differences, and so the size of the 10 × 10 × 10 cell was considered to be sufficient. Once the initial simulation box is built, the Monte Carlo method proceeds via the following steps: (1) swap two cations, (2) characterize the new Li environments, and (3) accept or reject the move according to a set of chosen rules. The swaps can be done between Li, Mn, and Ti belonging to octahedral sites (or to tetrahedral sites) or between cations belonging to different structural sites. If the simulations are done without constraints, all the swaps will be done randomly. If the simulations are done under constraints, the swaps which do not lead to Li environments conflicting with the set constraints will always be accepted, while the swaps leading to unwanted Li environments will be accepted with a small probability. The acceptance probability of unwanted moves is $P_{acc} = exp(-E_a/k_BT)$. Here, for all simulations, E_a was taken to be 10 eV, i.e. the probability of having unwanted Li environments is very close to zero. In this work, the constraints are set based on the experimental ^7Li NMR isotropic shifts. For example, if the spectrum of a particular composition does not show peaks at negative shifts, this is used as a constraint in the Monte Carlo simulation, which associates a small probability to the Li environments calculated to have negative shifts.

In addition to the swaps between the cations present in the structure, the Monte Carlo moves can include changes between different cation types. This is needed to reach some of the intermediate x values in the series. For example, on going from $LiTi_{1.5}Mn_{0.5}O_4$ to $LiTi_{1.4}Mn_{0.6}O_4$, a number of Ti ions need to be replaced by Mn ions and some Mn^{2+} ions (the only Mn oxidation state possible for $LiTi_{1.5}Mn_{0.5}O_4$) will be converted to Mn^{3+} ions. These changes in cation types are also made with or without constraints. Once a satisfactory representation of the system has been reached, in terms of (i) Li distribution in Td and Oh sites and (ii) stoichiometry of the structure, the number of Li cations in each environment is simply counted, the corresponding shifts are calculated and, as in the random solution model representation, the simulated NMR spectrum is then obtained by summing the Gaussian plots corresponding to the various environments present in the system.

Model for Two Phase Systems. The random solution model and Monte Carlo approaches described above were first used to simulate homogeneous (single-phase) systems. In the $LiTi_xMn_{2-x}O_4$ series, this single phase representation is able to depict only part of the series of materials. To investigate the possibility of having inhomogeneous

systems, we simulated independently two single-phase NMR spectra and summed them according to the fractions of the structure corresponding to each of the phases present in the system. In the Monte Carlo simulations, we built a single simulation box with two regions, each of the regions corresponding to a given phase.

■ RESULTS AND DISCUSSION

Geometry Optimization and Energy Profile. Figure 2 compares the formation energies of a number of structures in
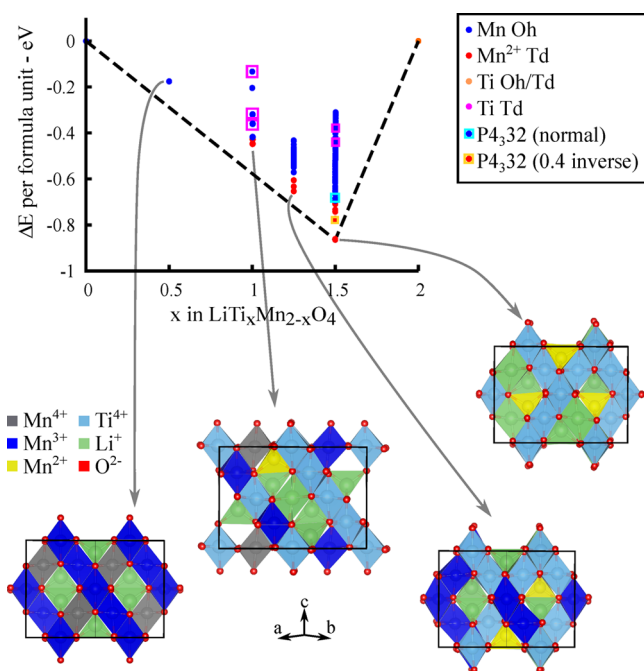
Figure 2. Formation energy per $LiTi_xMn_{2-x}O_4$ formula unit vs fractional Ti concentration (x) in the $LiTi_xMn_{2-x}O_4$ series. The convex hull is indicated with a dashed line. Insets show the minimum-energy structure for each of the studied points of the series. The majority of the structures with energies plotted have Ti^{4+} ions on octahedral sites; those with Ti^{4+} on tetrahedral sites are indicated by blue circles corresponding to Oh Mn and outer magenta squares corresponding to Td Ti.

the $LiTi_xMn_{2-x}O_4$ series with formation energies below 0 eV, which are all obtained using the search strategy described in the previous section. The full set of simulated structures is shown in Figure S1 of the Supporting Information. The convex hull (tie-line in Figure 2) is obtained by joining the stable structures obtained by the search. The $LiTi_{1.5}Mn_{0.5}O_4$ phase corresponds to the bottom of the hull with the lowest energy configuration having all the Mn^{2+} ions on tetrahedral sites, in agreement with the results of Petrov et al. based on X-ray diffraction.[16] This configuration corresponds to the phase having a 1:1 $Mn^{2+}:Li^+$ mixed occupancy of the Td sites, and a 0.75:0.25 $Ti^{4+}:Li^+$ mixed occupancy of the Oh sites, i.e., in the $A[B_2]O_4$ notation, $Li_{0.5}Mn_{0.5}[Li_{0.5}Ti_{1.5}]O_4$, with cubic $P4_332$ space group symmetry. For stoichiometries with $x > 1.0$, which have mixed $Mn^{2+}-Mn^{3+}$ oxidation states, the lowest energy structures are the ones having Mn^{2+} ions on tetrahedral sites and Mn^{3+} and Ti^{4+} on octahedral sites, consistent with previous X-ray diffraction results.[16] For stoichiometries of $0.2 \leq x < 1.0$, which have mixed $Mn^{3+}-Mn^{4+}$ oxidation states, the lowest energy structures are the ones having full Li occupancy of the tetrahedral $8a$ sites, and $Mn^{3+}-Mn^{4+}-Ti^{4+}$ on the octahedral

$16d$ sites. For the case of $x = 1.0$, the normal spinel $(Li[TiMn^{3+}]O_4)$ has all Mn ions nominally in the 3+ oxidation state. Our results show that this ordering does not correspond to the lowest energy structure of this composition. We find that the thermodynamically favorable ordering for $x = 1.0$ is the partially inverse spinel with mixed $Li-Mn^{2+}$ occupancy of the tetrahedral ($8a$) sites and mixed $Li-Mn^{3+}-Mn^{4+}-Ti^{4+}$ occupancy of the octahedral ($16d$) sites, in agreement with previous X-ray diffraction studies.[15,16] The mixed Mn oxidation state in the inverse spinel results from the charge disproportionation of $Mn^{3+}_{(8a)}+Mn^{3+}_{(16d)} \rightarrow Mn^{2+}_{(8a)}+Mn^{4+}_{(16d)}$, in agreement with the preferential occupancy of the Td ($8a$) sites by Mn^{2+} over Mn^{3+}.[15,16] Our results show that configurations with mixed $Li-Ti$ occupancy of the tetrahedral sites and mixed $Li-Mn^{3+}-Ti$ occupancy of the octahedral sites are thermodynamically unfavorable. This is in agreement with the XRD studies of Petrov et al.[16] and Krins et al.[15] A recent work by Murphy et al.[17] based on synchrotron X-ray and neutron powder diffraction, however, indicated partial occupancy of Ti in the tetrahedral sites of the $LiTiMnO_4$ lattice, which was not reported in the previous studies[15,16] nor reproduced by our DFT results.

According to the presented analysis based on the calculated formation energies, we can gain some insights into the more stable cation distributions in the spinel lattice, and the results we work with are gathered in Table 1.

Table 1. Summary of the Energetically Favorable Tetrahedral (Td) and Octahedral (Oh) Occupancies Obtained from the DFT Analysis of the Formation Energies throughout the $LiTi_xMn_{2-x}O_4$ Series

x in $LiTi_xMn_{2-x}O_4$					
$0.2 \leq x < 1.0$		$x = 1.0$		$1.1 \leq x \leq 1.5$	
Td sites	Oh sites	Td sites	Oh sites	Td sites	Oh sites
Li^+	Mn^{3+}	Li^+	Li^+	Li^+	Li^+
	Mn^{4+}	Mn^{2+}	Mn^{3+}	Mn^{2+}	Mn^{2+}
	Ti^{4+}		Mn^{4+}		Mn^{3+}
			Ti^{4+}		Ti^{4+}

Solid-State NMR. Full one-dimensional ^7Li double-adiabatic spin−echo[31] spectra of the $LiTi_xMn_{2-x}O_4$ powder samples ($0.2 \leq x \leq 1.5$) are given in Figure 3a. The double-adiabatic spin−echo sequence was chosen to obtain an efficient inversion of the whole spinning-sideband pattern, here of more than 400 kHz width.[50] The corresponding central regions of the spectra are shown in Figure 3b. The intensity ratio between the centerband and the sidebands did not change across the spectra, and for this reason we fit only the isotropic resonances. The variety of Li environments occurring in each phase leads to multiple distinct resonances and a broad isotropic region. The resonances, on average, range from around 500 to 30 ppm with the increase in Ti concentration. We also note that the spectrum is significantly broader for intermediate x values with the central regions covering a range of almost 600 ppm for $0.6 \leq x \leq 1.0$.

The distribution of discrete resonances giving rise to the broad spectra observed are due to Li ions in different local environments. These Li ions have different numbers of Mn^{2+}, Mn^{3+}, and Mn^{4+} ions in their local coordination sphere, each contributing differently to the ^7Li Fermi contact shift. The shifting of the resonances to lower frequency with the increasing Ti concentration is consistent with the decrease in
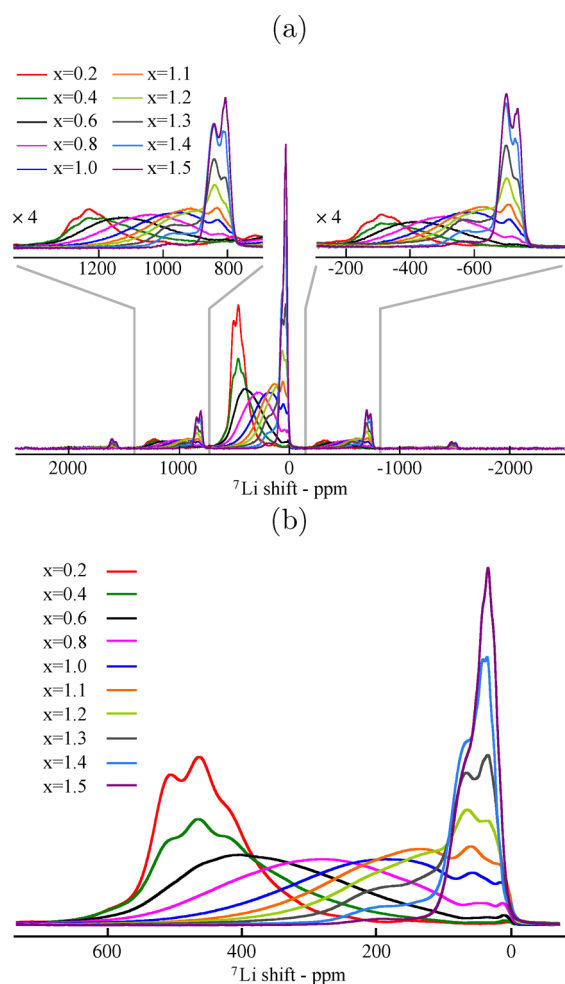
Figure 3. (a) ^{7}Li NMR spectra of the LiTi$_x$Mn$_{2-x}$O$_4$ series with the first-order sidebands enlarged in the top insets. (b) Expanded view of the isotropic resonances of the spectra.

the average Mn oxidation state and the decrease in the overall concentration of paramagnetic Mn ions.[28] A more detailed understanding of the structural differences across the series is now presented based on the DFT analysis of the Fermi contact interaction.

DFT Calculation of Magnetic and Hyperfine Parameters. As described previously (eq 3), the magnetic scaling of the hyperfine interaction was modeled via a mean field approach based on the exchange coupling interaction between Mn pairs, as shown in Figure 4. Mn^{3+} has a $(t_{2g})^3 (e_g^*)^1$
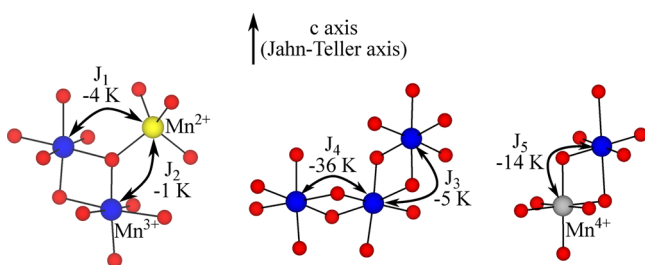
Figure 4. Mn−Mn exchange coupling constants identified in the studied systems, i.e. LiTi$_{1.25}$Mn$_{0.25}$O$_4$ for J_1 and J_2, LiTiMnO$_4$ for J_3 and J_4, and LiTi$_{0.5}$Mn$_{1.5}$O$_4$ for J_5. For each J_n, the reported value corresponds to the average between the HYB20-HYB35 results.

electronic configuration, which makes it Jahn−Teller active. Consequently, different exchange couplings and Fermi contact interactions were identified, depending on whether the pathway involves the Jahn−Teller lengthened or shortened Mn−O bond. The calculated J_n values are presented in Table 2. The

Table 2. Comparison of the Calculated Mn−Mn Exchange Coupling Constants for Pairs of Ions Interacting via an Oxygen Bridge[a]

J type	magnetic interaction	Mn−Mn angle (°)	J_{exc} (K)	
			HYB20	HYB35
J_1	Mn^{2+}−Mn^{3+} JT short	120.2	−5	−3
J_2	Mn^{2+}−Mn^{3+} JT long	120.1	−1	−1
J_3	Mn^{3+}−Mn^{3+} JT short−JT long	90.6	−8	−3
J_4	Mn^{3+}−Mn^{3+} JT short−JT short	97.2	−41	−32
J_5	Mn^{4+}−Mn^{3+} JT short−JT long	96.1	15	13

[a]For the couplings involving Mn^{3+} ions, the nature of Jahn−Teller shortened or lengthened bond involved in the interaction is also specified. The results obtained with the HYB20 and HYB35 hybrid functionals are shown separately. Different J_n types are labeled as in Figure 4.

results agree well with the values reported by Lee et al. and Clément et al. for similar Mn oxides such as MgMn$_2$O$_4$[33] and NaMnO$_2$.[32] Additionally, the accuracy of the calculated exchange integrals is tested for the LiTi$_{0.4}$Mn$_{1.6}$O$_4$ case by comparing the magnetic scaling factors obtained with the mean field approach and using the experimental magnetic susceptibility. The computational and experimental results obtained are in good agreement, and the details of the comparison are presented in the Supporting Information. The magnitude of the exchange interactions is sensitive to the distance between the coupled ions as well as to the coupling mechanism between the involved orbitals. As an example, we compare the exchange interactions between Mn^{3+}−Mn^{3+} in octahedral sites. The J_4 coupling (Figure 4, center) involves four Jahn−Teller shortened Mn−O bonds which allow direct overlap between the Mn t_{2g} orbitals, leading to a strong antiferromagnetic exchange interaction. The J_3 coupling (Figure 4, center) involves two Jahn−Teller shortened and two Jahn−Teller elongated Mn−O bonds, the latter ones reducing the direct overlap between t_{2g} orbitals and hence the strength of the direct exchange interaction. The superexchange interaction between the orbitals along the Jahn−Teller axis (d_{z^2}−$d_{xz/yz}$) results in a combination of weak ferro- and antiferromagnetic interactions, resulting in a significantly smaller J_3 coupling that is antiferromagnetic overall.

The possible Mn−O−Li bond pathways were identified for Li occupying Td as well as Oh sites. All the Li environments and corresponding pathways are described in Figure 5 and are presented in Table 3. As rationalized by Carlier et al.,[51] the transfer of paramagnetic electron spin from the Mn t_{2g}/e_g^* orbitals to the s orbitals of the Li occur primarily via a superexchange-like mechanism. As presented in eq 1, the sign and magnitude of the Fermi contact shift are determined by a combination of factors. The extent of the transferred spin density as well as the strength of the magnetic interaction discussed previously strongly depend on the bond distances between the involved sites and on the orbitals involved in the interaction.[51] The Mn−O−Li pathways in these systems
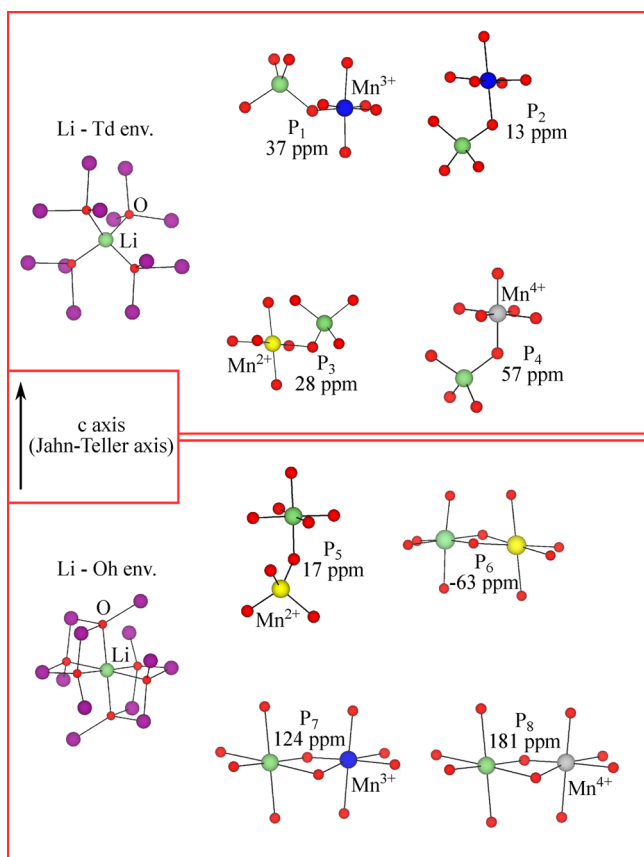
Figure 5. ^{7}Li bond pathway contributions to the Fermi contact shift for a lithium center (in green) in a tetrahedral site (top) or in a octahedral site (bottom), each coordinated by 12 TM sites (in purple) via oxygen (in red) bonds. Manganese is shown in yellow, blue, and gray for Mn^{2+}, Mn^{3+}, and Mn^{4+}, respectively. For each bond pathway contribution P, the reported value corresponds to the average between the HYB20-HYB35 results.

involve intermediate angles (neither exactly 90° nor exactly 180°); hence, the spin-density transfer deviates from a pure delocalization/polarization mechanism, and a complex combination of both processes is expected to occur. Nonetheless, we take the Li−O−Mn^{3+} pathways P_1 and P_2 (Figure 5, top) as examples to give an approximate rationalization of the mechanisms involved. The P_1 pathway involves the Jahn−Teller shortened Mn−O bond with positive transfer of spin density from the d_{xy} orbital via a delocalization mechanism. The

P_2 pathway involves the Jahn−Teller lengthened Mn−O bond, and a combination of positive delocalization transfer from the $d_{xz/yz}$ orbitals and a negative polarization transfer from the d_{z^2} orbital results in a weaker net Fermi contact interaction with the Li site.
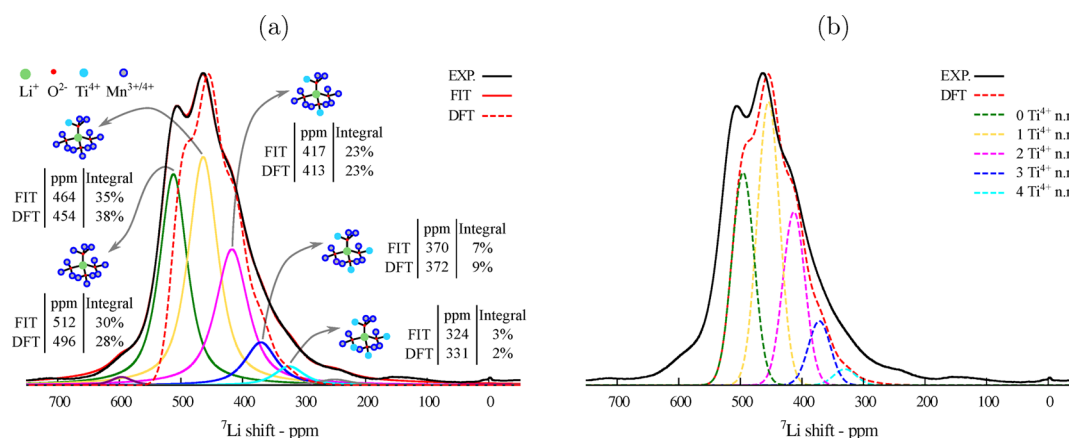
Simulation and Fitting of the Experimental ^{7}Li NMR Spectra. We now demonstrate how the bond pathway contributions calculated in Table 3 can be used to model the ^{7}Li NMR spectra of the $LiTi_xMn_{2-x}O_4$ series, allowing us to extract detailed local structural information. The shift values calculated with the HYB20 and HYB35 functionals give the upper and lower bounds; however, in the following analysis, we use a pragmatic approach in which the HYB20 and HYB35 results are averaged to give a single value for each pathway P, as shown in Table 3. For all the systems containing Mn^{3+}, we model the Jahn−Teller distortion as a dynamic process in which the time scale of the changes in local Mn−O bond lengths is much faster than the typical NMR time scale.[29] As a consequence, we assume that the shifts corresponding to Mn^{3+}−O−Li are well-represented by a weighted average with $^2/_3$ of Jahn−Teller-short and $^1/_3$ of Jahn−Teller-long pathway contributions.[29]

For all the systems containing exclusively Mn^{3+} and Mn^{4+} ions, i.e. the $0.2 \leq x \leq 0.8$ stoichiometries, we make an additional assumption. In this case, we consider that the time scale of electronic conduction is fast compared to the NMR time scale. This means that we can consider only one shift corresponding to an average oxidation state of the Mn ions. The weighted average depends on the stoichiometry of the system, as the average oxidation state is a function of the Ti content of the material. For example, for $LiTi_{0.2}Mn_{1.8}O_4$, the average Mn oxidation state is 3.444, while it is 3.375 for $LiTi_{0.4}Mn_{1.6}O_4$. As a result, the net shift contributions are 41 ppm for a $Mn^{3.44+}$ in $LiTi_{0.2}Mn_{1.8}O_4$, 39 ppm for a $Mn^{3.38+}$ in $LiTi_{0.4}Mn_{1.6}O_4$, 37 ppm for a $Mn^{3.29+}$ in $LiTi_{0.6}Mn_{1.4}O_4$, and 33 ppm for a $Mn^{3.17+}$ in $LiTi_{0.8}Mn_{1.2}O_4$. This assumption, as well as the accuracy of the calculated bond pathway shift contributions is tested with respect to the ^{7}Li NMR shift of $LiMn_2O_4$. This material has been extensively studied with NMR: as discussed in detail by Lee et al.,[18] the NMR spectrum of $LiMn_2O_4$ with Li in the tetrahedral 8a position is dominated by one major resonance with an isotropic shift of 512−520 ppm, the exact value varying between samples and likely the temperature of the measurement. In this stoichiometry, Mn is present in an average oxidation state of 3.5+. Combining the shift contributions that we obtained with DFT, summarized in

Table 3. Comparison of the Calculated Mn−O−Li Pathway Contributions to the ^{7}Li Fermi Contact Shift Obtained with Either the HYB20 or HYB35 Functional[a]

Li environment	pathway	Mn neighbor	Mn−Li distance (Å)	Mn−O−Li angle (°)	shift H20; H35 (ppm)	average shift (ppm)
Li Td	P_1	Mn^{3+} Oh JT short	3.5	120.2	34; 39	37
	P_2	Mn^{3+} Oh JT long	3.6	114.0	10; 16	13
	P_3	Mn^{2+} Oh	3.5	115.2	24; 32	28
	P_4	Mn^{4+}	3.5	116.2	50; 64	57
Li Oh	P_5	Mn^{2+} Td	3.5	114.0	15; 18	17
	P_6	Mn^{2+} Oh	3.0	92.3	−54; −73	−64
	P_7	Mn^{3+} Oh JT long	3.6	91.6	150; 98	124
	P_8	Mn^{4+} Oh	3.5	92.0	213; 151	181

[a]The table rows on the top (P_1 to P_4) show the possible neighboring TM sites transferring unpaired-electron spin density to a Li center in a tetrahedral site, while the table rows on the bottom (P_5 to P_8) show the possible sites transferring unpaired-electron spin density to a Li center in an octahedral site. Pathways are labelled as in Figure 5.

Figure 6. (a) Comparison of the experimental isotropic region of the ^{7}Li NMR spectrum of $LiTi_{0.2}Mn_{1.8}O_4$ (in black with the fitting shown in red) and the DFT-simulated resonance assuming a random distribution of Ti^{4+} and $Mn^{3+/4+}$ (in dashed red). Also shown are the peaks used in the fitting of the experimental spectrum (purple, green, yellow, magenta, blue, cyan, and gray peaks). (b) For comparison, the peaks obtained in the DFT-simulated random distribution model are shown, following the same coloring scheme as in panel (a).

Table 3, and accounting for a dynamic Jahn–Teller distortion, our calculations predict a net shift contribution of 43 ppm from a $Mn^{3.5+}$ ion. Given that in the $LiMn_2O_4$ spinel structure each Li is bonded via the oxygen to 12 Mn ions, the overall calculated Li NMR shift is $12 \times 43 = 515$ ppm, in very good agreement with the experimental shift.[18]

$LiTi_{0.2}Mn_{1.8}O_4$. We begin our analysis of the NMR results by considering the member of the series with the lowest Ti concentration, i.e. $LiTi_{0.2}Mn_{1.8}O_4$. For this system, the ^{7}Li NMR spectrum was simulated assuming a random distribution of ions in the Li local coordination shell. All Li ions were placed on the tetrahedral sites, following our observation that the presence of Ti^{4+}, Mn^{3+}, and Mn^{4+} on tetrahedral sites is energetically unfavorable. The total DFT predicted spectrum is shown in Figure 6a with the individual peaks shown in Figure 6b. The spectrum is obtained as a Gaussian distribution of resonances corresponding to each Li environment with the associated total Fermi contact shift obtained as a sum of the DFT-calculated pathway contributions. The Li environment corresponding to each resonance differs from the others by the number of Ti centers among the 12 neighboring sites.

The experimental ^{7}Li NMR spectrum of $LiTi_{0.2}Mn_{1.8}O_4$ was then fitted, as shown in Figure 6a. A good fit is obtained by using five more intense peaks of Voigt line shape and two very weak peaks. The shift contributions predicted with DFT match very well with the values obtained from the experimental fit with a maximum discrepancy of 16 ppm. The 5 main peaks extracted from the fit are assigned to Li sites with 12 Mn neighbors (fit: 512 ppm, DFT: 496 ppm), 11 Mn and 1 Ti neighbors (fit: 464 ppm, DFT: 454 ppm), 10 Mn and 2 Ti neighbors (fit: 417 ppm, DFT: 413 ppm), 9 Mn and 3 Ti neighbors (fit: 370 ppm, DFT: 372 ppm), and 8 Mn and 4 Ti (fit: 324 ppm, DFT: 331 ppm), as shown in Figure 6a. Moreover, the relative intensities of the different peaks are accurately reproduced by the model that considers a random distribution of Ti^{4+} and $Mn^{3.44+}$ among the octahedral sites. The weak peak at 595 ppm is also predicted by DFT with the model that does not consider a dynamic exchange between Mn^{3+} and Mn^{4+}. In particular, the shift of the Li environment coordinated with 3 Mn^{3+} and 9 Mn^{4+} is calculated to be 599 ppm, in good agreement with the experimental shift of 595 ppm.

Figure S2 in the Supporting Information shows the results of the model that does not consider a dynamic exchange between Mn^{3+} and Mn^{4+}. The line shape of the spectrum simulated in this way is not in as good of agreement with the experimental NMR spectrum, confirming that the fast $Mn^{3+/4+}$ hopping rate in the experimental NMR conditions is a good assumption for these systems.

$0.4 \leq x < 1.0$ Stoichiometries. Following the successful description of the cation ordering for $LiTi_{0.2}Mn_{1.8}O_4$ with the random distribution model, we apply the same approach for the $0.4 \leq x < 1.0$ stoichiometries. As shown in Figure S3 of the Supporting Information, the deconvolution of the isotropic region for $LiTi_{0.4}Mn_{1.6}O_4$ deviates significantly from the spectrum simulated for the random distribution model. The disagreement between the experimental NMR spectra and the simulations based on the random distribution model persists for all the $0.4 \leq x < 1.0$ cases, as shown in Figure S4 of the Supporting Information.

By comparing the NMR fit of the isotropic region for $LiTi_{0.2}Mn_{1.8}O_4$ (Figure 6a) and that of $LiTi_{0.4}Mn_{1.6}O_4$ (Figure S3), we notice that (i) the major contributing peaks of the $x = 0.2$ spectrum have the same shifts as 5 of the major peaks in the $x = 0.4$ case and (ii) the spectrum of the $x = 0.4$ case shows an additional broad feature that extends between 300 and 100 ppm, which is absent in the spectrum of $x = 0.2$. In $LiTi_{0.2}Mn_{1.8}O_4$, Mn has a net charge of 3.44+, while in $LiTi_{0.4}Mn_{1.6}O_4$, Mn has a net charge of 3.375+, each with different Fermi contact shift contributions to the neighboring Li center (41 ppm for $Mn^{3.44+}$ and 39 ppm for $Mn^{3.375+}$). The fact that the fits of the spectra for the $x = 0.2$ and for the $x = 0.4$ cases give the major peaks at exactly the same shifts indicate that in the $x = 0.4$ cases these correspond to Mn^{4+}-rich Li environments. The spectrum of the $x = 0.4$ case simulated for the random $Mn^{3.375+}$–Ti distribution does not show shifts lower than 240 ppm, in disagreement with the experimental spectrum. This suggests the presence of Mn^{3+}-rich Li environments in the structure. The ^{7}Li isotropic region for $LiTi_{0.4}Mn_{1.6}O_4$ is hence modeled as a 1:1 combination (i.e., an average) of the $LiTi_{0.2}Mn_{1.8}O_4$ and $LiTi_{0.6}Mn_{1.4}O_4$ experimental spectra. The resulting peaks, shown in Figure 7, reproduce the experimental spectrum of the $x = 0.4$ case very well, indicating a coexistence of Mn^{4+}-rich and Mn^{3+}-rich domains.

The spectra for the $x = 0.6$ and 0.8 show a gradual shift of resonances toward lower frequency with the increasing Ti
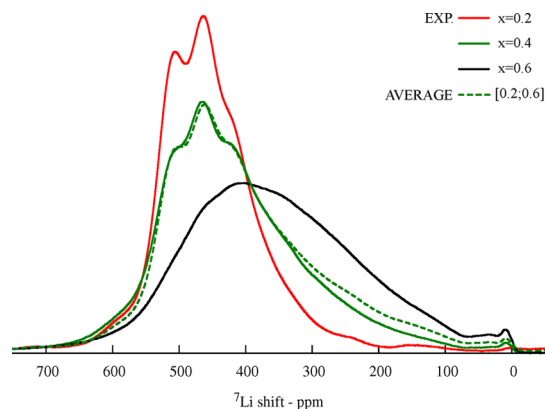
Figure 7. Comparison of the experimental isotropic region of the ^{7}Li NMR spectrum of $LiTi_{0.2}Mn_{1.8}O_4$ (in red), $LiTi_{0.4}Mn_{1.6}O_4$ (in green), and $LiTi_{0.6}Mn_{1.4}O_4$ (in black), and the calculated $LiTi_{0.4}Mn_{1.6}O_4$ (in dashed green) isotropic peak. This is obtained by taking the average of the peaks of $x = 0.2$ and 0.6.

concentration, indicative of a continuous solid solution behavior.[16]

LiTiMnO$_4$. As described in Figure 2 and in Table 1, for the x = 1 case, our calculations predicted that the configuration with mixed $Li–Mn^{2+}$ tetrahedral and $Li–Mn^{3+/4+}–Ti$ octahedral occupancies is more favorable than the normal spinel $(Li[Mn^{3+}Ti]O_4)$. Studies based on X-ray diffraction reported 20–30% Li occupancy of the Oh site (or, equivalently, 20–30% Mn^{2+} on the Td site).[15,16] In an attempt to model the spectrum for $LiTiMnO_4$, we hence consider a random cation distribution for the normal spinel lattice $(Li[Mn^{3+}Ti]O_4)$ as well as for the partially inverse lattice with 30% site inversion $(Li_{0.7}Mn^{2+}_{0.3}[Li_{0.3}Mn^{4+}_{0.3}Mn^{3+}_{0.4}Ti]O_4)$. The results are shown in Figure 8.

The spectrum simulated for the partially inverse case (Figure 8b) shows shifts over the entire 0–700 ppm region of the experimental spectrum, while the simulation for the normal spinel (Figure 8a) shows shifts only between 20–300 ppm. This confirms the presence of both Li(Td) and Li(Oh) environments in the structure, as predicted by our calculations (Table 1). However, the line shape of the experimental

spectrum is not well reproduced by the simulation for the disordered $Li_{0.7}Mn^{2+}_{0.3}[Li_{0.3}Mn^{3+}_{0.4}Mn^{4+}_{0.3}Ti]O_4$ lattice, particularly between 0–100 and 350–450 ppm. This indicates that the cations are not distributed randomly in the structure, and cation ordering determines the preferential presence of certain environments over others. Due to the configurational complexity of the system, which contains $Li/Mn^{2+,3+,4+}/Ti$ ions and mixed occupancy of the Td and Oh sites, further work would be needed to systematically analyze the configurational energies of different orderings[52] and possibly account for the electroneutrality principle.[53]

LiTi$_{1.5}$Mn$_{0.5}$O$_4$. We now turn to the interpretation of the NMR spectra for the Ti-rich part of the series, starting with the end member $LiTi_{1.5}Mn_{0.5}O_4$. In this system, we expect Li^+, Mn^{2+}, and Ti^{4+} cations to be present. The formation energies calculated with DFT shown in Figure 2 indicate that it is energetically favorable for Mn^{2+} ions to be on tetrahedral sites, leading to (at least) a fraction of the Li ions on the octahedral sites, also suggested by previous X-ray studies.[16] This fraction is referred to as the inverted fraction of Li, y, in the notation $Li_{1-y}Mn_y[Li_yTi_{1.5}Mn_{0.5-y}]O_4$. The first model we test is a random distribution of Mn^{2+}/Li^+ ions on tetrahedral sites and $Li^+/Mn^{2+}/Ti^{4+}$ on octahedral sites. The simulated NMR spectra are shown in Figure S5 of the Supporting Information for various inverted fractions of Li from $y = 0.0$ (i.e., $Li[Ti_{1.5}Mn_{0.5}]O_4$) to $y = 0.5$ (i.e., $Li_{0.5}Mn_{0.5}[Li_{0.5}Ti_{1.5}]O_4$). When the inverted fraction is $y = 0.5$, all Mn^{2+} are on tetrahedral sites; half of the Li ions are on octahedral sites, and half of the Li ions are on tetrahedral sites. None of the spectra show good agreement with the experiment. The simulated spectra show two main features in strong disagreement with the experimental data, i.e. resonances at 0 ppm and some at negative frequencies, which are clearly not present in the experimental NMR spectrum. To use this information, we thus turn to another strategy and follow an approach similar to reverse Monte Carlo, where constraints are imposed. We use as a starting point a spinel structure with a $P4_332$ symmetry, as this was suggested by X-ray studies on this material.[16] In our starting $P4_332$ structure, the lattice is characterized by a full Li occupancy on the tetrahedral sites and a full Ti/Mn occupancy of the octahedral sites (i.e., a regular spinel structure). This ordering corresponds to the

(a)   (b)
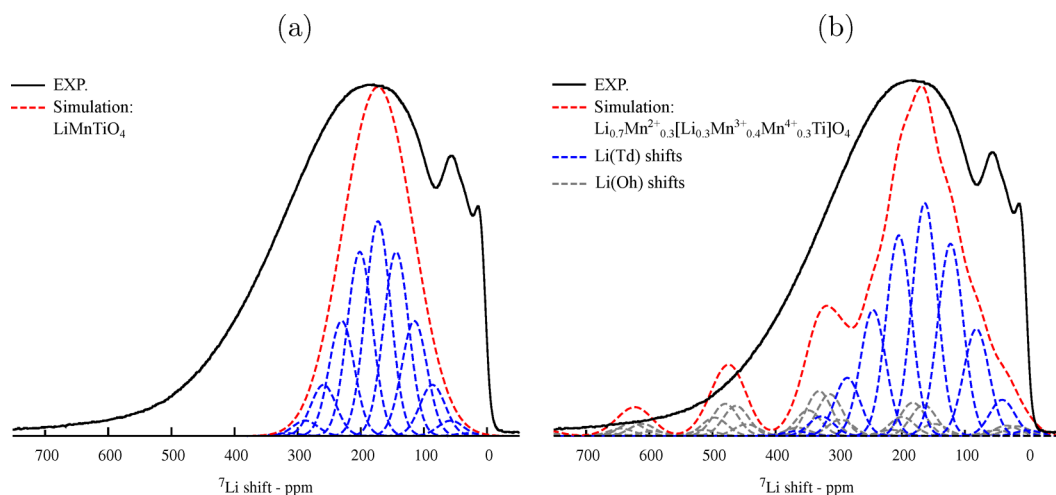
Figure 8. Comparison of the experimental isotropic region of the ^{7}Li NMR spectrum of $LiTiMnO_4$ (solid black line) with the simulated spectrum of the normal $Li[TiMn^{3+}]O_4$ (dashed red line, a), and the simulated spectrum of the partially inverse $Li_{0.7}Mn^{2+}_{0.3}[Li_{0.3}Mn^{3+}_{0.4}Mn^{4+}_{0.3}Ti]O_4$ (dashed red line, b). Also shown are the peaks corresponding to Li(Td) environments (dashed blue lines) and to Li(Oh) environments (dashed gray lines).
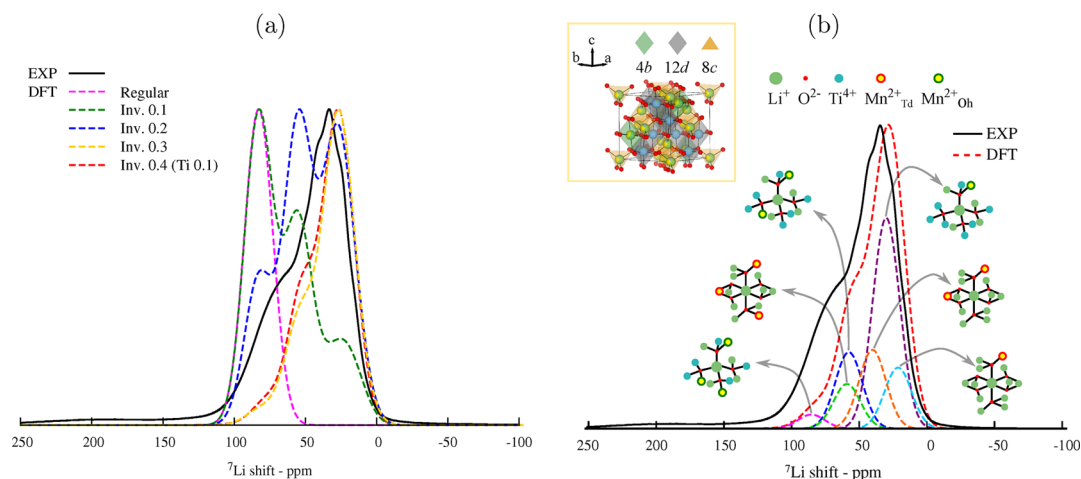
Figure 9. (a) Isotropic region of the experimental ^{7}Li NMR spectrum of LiTi$_{1.5}$Mn$_{0.5}$O$_4$ (solid black line), and the NMR results of the reverse Monte Carlo simulation of Li$_{1-y}$Mn$_y$[Li$_y$Ti$_{1.5}$Mn$_{0.5-y}$]O$_4$. Dotted magenta, green, blue, and yellow lines for y = 0, 0.1, 0.2, and 0.3, respectively, and the dotted red line for Li$_{0.6}$Ti$_{0.1}$Mn$_{0.3}$[Li$_{0.4}$Ti$_{1.4}$Mn$_{0.2}$]O$_4$. (b) Isotropic region of the experimental ^{7}Li NMR spectrum (in solid black line) and the simulated spectrum (in dotted red line) of Li$_{0.6}$Ti$_{0.1}$Mn$_{0.3}$[Li$_{0.4}$Ti$_{1.4}$Mn$_{0.2}$]O$_4$. For each Li coordination, the corresponding peak is shown, as calculated with the Monte Carlo method. The corresponding cation ordering in the $P4_332$ lattice is shown in the top-left inset.

presence of only one type of Li environment with 9 Ti^{4+} and 3 Mn$^{2+}_{Oh}$ neighbors. The calculated shift is 3 × 28 ppm = 85 ppm, in clear disagreement with the experimental NMR (Figure 9a). Starting from the fully regular structure, the Monte Carlo simulation then allowed for some fraction of Li to move onto the octahedral environment with the consequent swap of Mn (and Ti) onto the tetrahedral sublattice. After each swap, the Li coordination environments are checked, and the corresponding shifts are calculated. If the swap leads to a "wrong" shift (a shift ≤0 ppm), it will be accepted but only with a very low probability.

The results of the reverse Monte Carlo approach are shown in Figure 9a. The best agreement between simulation and experiment is obtained for the y = 0.4 case, shown more in detail in Figure 9b, corresponding to the Li$_{0.6}$Ti$_{0.1}$Mn$_{0.3}$[Li$_{0.4}$Ti$_{1.4}$Mn$_{0.2}$]O$_4$ lattice of $P4_332$ symmetry with the repeated unit shown in the inset of Figure 9b. The Li environments present in the lattice are also shown with the associated NMR peaks. The good agreement between the model and the experimental spectrum allows us to conclude that the spinel network of the LiTi$_{1.5}$Mn$_{0.5}$O$_4$ system, of $P4_332$ symmetry as previously reported,[16] contains mixed cation occupancy of Li, Mn^{2+}, and Ti in both tetrahedral and octahedral environments. The presented analysis also allows us to derive a specific cation ordering within $P4_332$ network, i.e. (Li$_{0.6}$Ti$_{0.1}$Mn$_{0.3}$)$_{8c}$[(Li$_{0.1}$Ti$_{1.4}$)$_{12d}$(Li$_{0.3}$Mn$_{0.2}$)$_{4b}$]O$_4$.

1.1 ≤ x ≤ 1.4 Stoichiometries. The reverse Monte Carlo approach was implemented further to analyze the NMR spectra of the intermediate 1.1 ≤ x ≤ 1.4 systems. We first look at the LiTi$_{1.4}$Mn$_{0.6}$O$_4$ material using exactly the same approach as for LiTi$_{1.5}$Mn$_{0.5}$O$_4$ but now having a mix of Mn^{3+} and Mn^{2+} ions. As highlighted previously from the DFT results, the presence of Mn^{3+} on tetrahedral sites is unfavorable. The NMR spectra simulated for a homogeneous LiTi$_{1.4}$Mn$_{0.6}$O$_4$ system and various inverted fractions are shown in Figure S6 of the Supporting Information. It is clear from the comparison with experiments that this model is not sufficient to describe the system. In particular, there is a broad peak with a large shift (~200 ppm) which cannot be explained by this model, while the region of the spectrum between 0−100 ppm decreases in

intensity but does not vary in shift compared to the LiTi$_{1.5}$Mn$_{0.5}$O$_4$ case.

To use this information, we modify the model to retain the $P4_332$ ordering of the Mn^{2+}-rich phase, as shown for the x = 1.5 case, while including a random distribution of cations in the $Fd\bar{3}m$ Mn^{3+}-rich phase, as shown for the 0.2 ≤ x ≤ 1.0 cases. In these simulations, a Gaussian width of 50 ppm was found to be required to model the $Fd\bar{3}m$ domain, while a Gaussian width of 12 ppm was again found to be sufficient to model the $P4_332$ domain. This difference between the peak widths may be rationalized in terms of the higher degree of disorder among the Li environments present in the $Fd\bar{3}m$ phase compared to the more ordered $P4_332$ phase. The approach is followed for the entire 1.1 ≤ x ≤ 1.4 series. Furthermore, for each composition, the Monte Carlo simulation also optimized the inverted fraction, y, within the $P4_332$ phase, and so we obtain for x = 1.4 Li$_{0.8}$Mn$^{2+}_{0.2}$[Li$_{0.2}$Mn$^{2+}_{0.2}$Mn$^{3+}_{0.2}$Ti$_{1.4}$]O$_4$, for x = 1.3 Li$_{0.86}$Mn$^{2+}_{0.14}$[Li$_{0.14}$Mn$^{2+}_{0.16}$Mn$^{3+}_{0.4}$Ti$_{1.3}$]O$_4$, for x = 1.2 Li$_{0.92}$Mn$^{2+}_{0.08}$[Li$_{0.08}$Mn$^{2+}_{0.12}$Mn$^{3+}_{0.6}$Ti$_{1.2}$]O$_4$. The results are shown in Figure 10. The good agreement between the simulated and the experimental NMR spectra throughout the 1.1 ≤ x ≤ 1.5 series suggests that as Mn^{2+} starts to be formed in the system, it preferentially occupies the tetrahedral environment, determining a partial ordering between Li−Mn^{2+} Td−Oh sites in the $P4_332$ symmetry, while the regular Mn^{3+}-rich component retains a random distribution of cations consistent with the $Fd\bar{3}m$ symmetry. As NMR probes structural short-range ordering, it does not allow us to distinguish the sizes of the $Fd\bar{3}m$ and the $P4_332$ phases. Because previous diffraction studies,[16] which are sensitive to long-range ordering, reported a single $P4_332$ phase behavior for 1.2 ≤ x ≤ 1.4, this may suggest that the $Fd\bar{3}m$−$P4_332$ phase segregation is on the local scale, potentially forming small domains.

The combination of first-principles shift calculations, random solution/Monte Carlo model, and experimental NMR enabled us to acquire a detailed understanding of the complex trend of cation ordering in the mixed LiTi$_x$Mn$_{2-x}$O$_4$ series. This is of particular interest in regards to the application of this material as a cathode in rechargeable Li-ion batteries. The high degree of cation disorder found at intermediate 0.2 ≤ x < 1 values of the
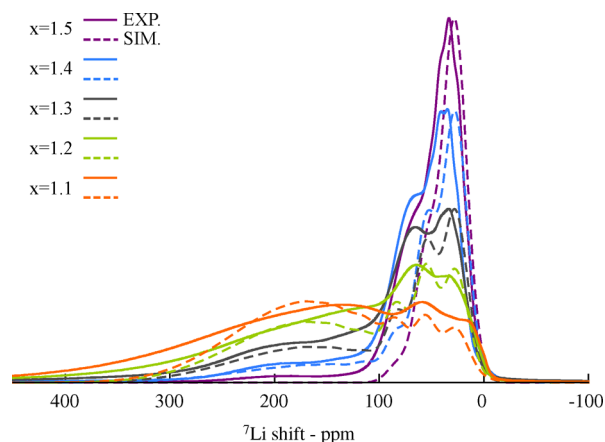
Figure 10. Comparison of the experimental isotropic region (solid line) of the ^{7}Li NMR spectrum of LiTi$_x$Mn$_{2-x}$O$_4$ and the simulated region (dashed line) assuming a distribution of Ti^{4+}, Mn^{2+}, and Mn^{3+} in a two-component model (purple, blue, gray, green, and orange for x = 1.5, 1.4, 1.3, 1.2, and 1.1, respectively).

series may hinder a cooperative Jahn−Teller distortion in the bulk and facilitate the mechanical stability during electrochemical cycling. On the other hand, the observed increasing ratio of Li(Oh)/Mn^{2+}(Td) mixing with increasing x may hinder the extraction of Li$^+$ from the structure, effectively resulting in a lower capacity.

CONCLUSIONS

A detailed solid-state ^{7}Li NMR and first-principles DFT study of the cation ordering and the structural changes in the LiTi$_x$Mn$_{2-x}$O$_4$ series ($0.2 \leq x \leq 1.5$) was presented. ^{7}Li MAS NMR spectra were obtained for the LiTi$_x$Mn$_{2-x}$O$_4$ series using state of the art spectroscopic methods for paramagnetic solids. The methodology used to analyze the NMR results involved the ab initio calculation of the magnetic and hyperfine parameters, obtaining a breakdown of the possible contributions to the ^{7}Li NMR shift. These were combined into random distribution and reverse Monte Carlo models to simulate the ^{7}Li NMR spectra of the LiTi$_x$Mn$_{2-x}$O$_4$ series. For x = 0.2, a random distribution of octahedral Mn$^{3+/4+}$/Ti^{4+} cations in the $Fd\bar{3}m$ structure was determined, evolving into an inhomogeneous lattice of Mn^{3+}-rich/Mn^{4+}-rich phases for x = 0.4 and a single-phase solid solution for x = 0.6 and 0.8. The x = 1.0 case showed partially inverse ordering of Mn$^{3+/4+}$−Ti^{4+}−Li (Oh) and Mn^{2+}−Li(Td) sites. In the $1.1 \leq x \leq 1.5$ structures, the results showed the preferential formation of coexisting disordered Mn^{3+}-rich ($Fd\bar{3}m$) and ordered Mn^{2+}-rich (partially inverse P4$_3$32) phases. Additionally, for LiTi$_{1.5}$Mn$_{0.5}$O$_4$, a specific cation ordering within the partially inverse spinel framework of P4$_3$32 symmetry was determined, i.e. (Li$_{0.6}$Ti$_{0.1}$Mn$_{0.3}$)$_{8c}$[(Li$_{0.1}$Ti$_{1.4}$)$_{12d}$(Li$_{0.3}$Mn$_{0.2}$)$_{4b}$]O$_4$. The ability of the DFT results to reproduce the experimental ^{7}Li NMR data is promising. The presented methodology in general and the DFT-calculated ^{7}Li NMR shifts in particular pave the way to a detailed rationalization of the solid-state NMR spectra of other paramagnetic solids. The combination of the calculated NMR shifts with the random distribution and reverse Monte Carlo methods represents a robust approach which can be extended to include additional energetic/configurational constraints to analyze other complex systems of interest to

the battery field such as LiZn$_x$Mn$_{2-x}$O$_4$, LiNi$_x$Mn$_{2-x}$O$_4$, and the Li-excess Li$_{1+\alpha}$Mn$_{2-\alpha}$O$_4$ materials.

ASSOCIATED CONTENT

Ⓢ Supporting Information

The Supporting Information is available free of charge on the ACS Publications website at DOI: 10.1021/acs.chemmater.7b04314.

Additional computational details, synthesis procedure, complete convex hull, additional lattice simulations, and details and results of magnetic SQUID measurements (PDF)

AUTHOR INFORMATION

Corresponding Author

*E-mail: cpg27@cam.ac.uk.

ORCID Ⓞ

Roberta Pigliapochi: 0000-0003-3714-8431
Siegbert Schmid: 0000-0002-5182-0725
Clare P. Grey: 0000-0001-5572-192X

Present Address

∥A.J.P.: Department of Materials and Environmental Chemistry, Stockholm University, Svante Arrhenius Väg 16 C, SE-106 91 Stockholm, Sweden.

Notes

The authors declare no competing financial interest.

REFERENCES

(1) Thackeray, M.; David, W.; Bruce, P.; Goodenough, J. Lithium insertion into manganese spinels. *Mater. Res. Bull.* **1983**, *18*, 461−472.

(2) Tarascon, J. M.; Wang, E.; Shokoohi, F.; McKinnon, W.; Colson, S. The Spinel Phase of LiMn$_2$O$_4$ as a Cathode in Secondary Lithium Cells. *J. Electrochem. Soc.* **1991**, *138*, 2859−2864.

(3) Hunter, J. C. Preparation of a new crystal form of manganese dioxide: λ-MnO$_2$. *J. Solid State Chem.* **1981**, *39*, 142−147.

(4) Goodenough, J. B.; Park, K.-S. The Li-ion rechargeable battery: a perspective. *J. Am. Chem. Soc.* **2013**, *135*, 1167−1176.

(5) Thackeray, M.; Johnson, P.; De Picciotto, L.; Bruce, P.; Goodenough, J. Electrochemical extraction of lithium from LiMn$_2$O$_4$. *Mater. Res. Bull.* **1984**, *19*, 179−187.

(6) Chan, H.; Duh, J.; Sheen, S. LiMn$_2$O$_4$ cathode doped with excess lithium and synthesized by co-precipitation for Li-ion batteries. *J. Power Sources* **2003**, *115*, 110−118.

(7) Rossouw, M.; De Kock, A.; De Picciotto, L.; Thackeray, M.; David, W.; Ibberson, R. Structural aspects of lithium-manganese-oxide electrodes for rechargeable lithium batteries. *Mater. Res. Bull.* **1990**, *25*, 173−182.

(8) Gao, Y.; Dahn, J. Synthesis and Characterization of Li$_{1+x}$Mn$_{2-x}$O$_4$ for Li-Ion Battery Applications. *J. Electrochem. Soc.* **1996**, *143*, 100−114.

(9) Xia, Y.; Yoshio, M. Optimization of Spinel Li$_{1+x}$Mn$_{2-y}$O$_4$ as a 4 V Li-Cell Cathode in Terms of a Li−Mn−O Phase Diagram. *J. Electrochem. Soc.* **1997**, *144*, 4186−4194.

(10) Gummow, R.; De Kock, A.; Thackeray, M. Improved capacity retention in rechargeable 4 V lithium/lithium-manganese oxide (spinel) cells. *Solid State Ionics* **1994**, *69*, 59−67.

(11) Zhong, Q.; Bonakdarpour, A.; Zhang, M.; Gao, Y.; Dahn, J. Synthesis and Electrochemistry of LiNi$_x$Mn$_{2-x}$O$_4$. *J. Electrochem. Soc.* **1997**, *144*, 205−213.

(12) Song, J.; Shin, D. W.; Lu, Y.; Amos, C. D.; Manthiram, A.; Goodenough, J. B. Role of Oxygen Vacancies on the Performance of Li[Ni$_{0.5-x}$Mn$_{1.5+x}$]O$_4$ (x = 0, 0.05, and 0.08) Spinel Cathodes for Lithium-Ion Batteries. *Chem. Mater.* **2012**, *24*, 3101−3109.

(13) Wang, S.; Yang, J.; Wu, X.; Li, Y.; Gong, Z.; Wen, W.; Lin, M.; Yang, J.; Yang, Y. Toward high capacity and stable manganese-spinel electrode materials: A case study of Ti-substituted system. *J. Power Sources* **2014**, *245*, 570−578.

(14) Duncan, H.; Hai, B.; Leskes, M.; Grey, C. P.; Chen, G. Relationships between Mn^{3+} Content, Structural Ordering, Phase Transformation, and Kinetic Properties in LiNi$_x$Mn$_{2-x}$O$_4$ Cathode Materials. *Chem. Mater.* **2014**, *26*, 5374−5382.

(15) Krins, N.; Hatert, F.; Traina, K.; Dusoulier, L.; Molenberg, I.; Fagnard, J.-F.; Vanderbemden, P.; Rulmont, A.; Cloots, R.; Vertruyen, B. LiMn$_{2-x}$Ti$_x$O$_4$ spinel-type compounds ($x \leq 1$): Structural, electrical and magnetic properties. *Solid State Ionics* **2006**, *177*, 1033−1040.

(16) Petrov, K.; Rojas, R. M.; Alonso, P. J.; Amarilla, J. M.; Lazarraga, M. G.; Rojo, J. M. Cation distribution and phase transformations in LiMn$_{2-y}$Ti$_y$O$_4$ ($0.2 \leq y \leq 1.5$) solid solutions. *Solid State Sci.* **2005**, *7*, 277−286.

(17) Murphy, D. T.; Schmid, S.; Hester, J. R.; Blanchard, P. E.; Miiller, W. Coordination Site Disorder in Spinel-Type LiMnTiO$_4$. *Inorg. Chem.* **2015**, *54*, 4636−4643.

(18) Lee, Y. J.; Wang, F.; Grey, C. P. 6Li and 7Li MAS NMR studies of lithium manganate cathode materials. *J. Am. Chem. Soc.* **1998**, *120*, 12601−12613.

(19) Grey, C. P.; Lee, Y. J. Lithium MAS NMR studies of cathode materials for lithium-ion batteries. *Solid State Sci.* **2003**, *5*, 883−894.

(20) Lee, Y. J.; Park, S.-H.; Eng, C.; Parise, J. B.; Grey, C. P. Cation Ordering and Electrochemical Properties of the Cathode Materials LiZn$_x$Mn$_{2-x}$O$_4$, $0 < x \leq 0.5$: A ^{6}Li Magic-Angle Spinning NMR Spectroscopy and Diffraction Study. *Chem. Mater.* **2002**, *14*, 194−205.

(21) Lee, Y. J.; Grey, C. P. Determining the lithium local environments in the lithium manganates LiZn$_{0.5}$Mn$_{1.5}$O$_4$ and Li$_2$MnO$_3$ by analysis of the ^{6}Li MAS NMR spinning sideband manifolds. *J. Phys. Chem. B* **2002**, *106*, 3576−3582.

(22) Lee, Y. J.; Eng, C.; Grey, C. P. 6Li Magic Angle Spinning NMR Study of the Cathode Material LiNi$_x$Mn$_{2-x}$O$_4$: The Effect of Ni Doping on the Local Structure during Charging. *J. Electrochem. Soc.* **2001**, *148*, A249−A257.

(23) Lee, Y. J.; Grey, C. P. ^{6}Li Magic Angle Spinning Nuclear Magnetic Resonance Study of the Cathode Materials Li$_{1+a}$Mn$_{2-a}$O$_{4-\delta}$ The Effect of Local Structure on the Electrochemical Properties. *J. Electrochem. Soc.* **2002**, *149*, A103−A114.

(24) Zhou, L.; Leskes, M.; Ilott, A. J.; Trease, N. M.; Grey, C. P. Paramagnetic electrodes and bulk magnetic susceptibility effects in the in situ NMR studies of batteries: Application to Li$_{1.08}$Mn$_{1.92}$O$_4$ spinels. *J. Magn. Reson.* **2013**, *234*, 44−57.

(25) McConnell, H. M.; Chesnut, D. B. Theory of Isotropic Hyperfine Interactions in π-Electron Radicals. *J. Chem. Phys.* **1958**, *28*, 107−117.

(26) McConnell, H. M.; Robertson, R. E. Isotropic nuclear resonance shifts. *J. Chem. Phys.* **1958**, *29*, 1361−1365.

(27) Kurland, R. J.; McGarvey, B. R. Isotropic NMR shifts in transition metal complexes: the calculation of the Fermi contact and pseudocontact terms. *J. Magn. Reson.* **1970**, *2*, 286−301.

(28) Grey, C. P.; Dupré, N. NMR Studies of Cathode Materials for Lithium-Ion Rechargeable Batteries. *Chem. Rev.* **2004**, *104*, 4493−4512.

(29) Middlemiss, D. S.; Ilott, A. J.; Clément, R. J.; Strobridge, F. C.; Grey, C. P. Density functional theory-based bond pathway decompositions of hyperfine shifts: Equipping solid-state NMR to characterize atomic environments in paramagnetic materials. *Chem. Mater.* **2013**, *25*, 1723−1734.

(30) Clément, R. J.; Pell, A. J.; Middlemiss, D. S.; Strobridge, F. C.; Miller, J. K.; Whittingham, M. S.; Emsley, L.; Grey, C. P.; Pintacuda, G. Spin-transfer pathways in paramagnetic lithium transition-metal phosphates from combined broadband isotropic solid-state MAS NMR spectroscopy and DFT calculations. *J. Am. Chem. Soc.* **2012**, *134*, 17178−17185.

(31) Pell, A. J.; Pintacuda, G. Broadband solid-state MAS NMR of paramagnetic systems. *Prog. Nucl. Magn. Reson. Spectrosc.* **2015**, *84*, 33−72.

(32) Clément, R. J.; Middlemiss, D. S.; Seymour, I. D.; Ilott, A. J.; Grey, C. P. Insights into the Nature and Evolution upon Electro-chemical Cycling of Planar Defects in the β-NaMnO$_2$ Na-Ion Battery Cathode: An NMR and First-Principles Density Functional Theory Approach. *Chem. Mater.* **2016**, *28*, 8228−8239.

(33) Lee, J.; Seymour, I. D.; Pell, A. J.; Dutton, S. E.; Grey, C. P. A systematic study of ^{25}Mg NMR in paramagnetic transition metal oxides: applications to Mg-ion battery materials. *Phys. Chem. Chem. Phys.* **2017**, *19*, 613−625.

(34) Kervern, G.; Pintacuda, G.; Emsley, L. Fast adiabatic pulses for solid-state NMR of paramagnetic systems. *Chem. Phys. Lett.* **2007**, *435*, 157−162.

(35) Hwang, T.-L.; Van Zijl, P. C.; Garwood, M. Fast broadband inversion by adiabatic pulses. *J. Magn. Reson.* **1998**, *133*, 200−203.

(36) Massiot, D.; Fayon, F.; Capron, M.; King, I.; le Calvé, S.; Alonso, B.; Durand, J.-O.; Bujoli, B.; Gan, Z.; Hoatson, G. Modelling one-and two-dimensional solid-state NMR spectra. *Magn. Reson. Chem.* **2002**, *40*, 70−76.

(37) Grau-Crespo, R.; Hamad, S.; Catlow, C.; De Leeuw, N. Symmetry-adapted configurational modelling of fractional site occupancy in solids. *J. Phys.: Condens. Matter* **2007**, *19*, 256201.

(38) Van der Ven, A.; Thomas, J. C.; Xu, Q.; Swoboda, B.; Morgan, D. Nondilute diffusion from first principles: Li diffusion in Li$_x$TiS$_2$. *Phys. Rev. B: Condens. Matter Mater. Phys.* **2008**, *78*, 104306.

(39) Van der Ven, A.; Thomas, J.; Xu, Q.; Bhattacharya, J. Linking the electronic structure of solids to their thermodynamic and kinetic properties. *Mathematics and Computers in Simulation* **2010**, *80*, 1393−1410.

(40) Perdew, J. P.; Burke, K.; Ernzerhof, M. Generalized gradient approximation made simple. *Phys. Rev. Lett.* **1996**, *77*, 3865.

(41) Kresse, G.; Furthmüller, J. Efficient iterative schemes for ab initio total-energy calculations using a plane-wave basis set. *Phys. Rev. B: Condens. Matter Mater. Phys.* **1996**, *54*, 11169.

(42) Blöchl, P. E. Projector augmented-wave method. *Phys. Rev. B: Condens. Matter Mater. Phys.* **1994**, *50*, 17953.

(43) Anisimov, V. I.; Zaanen, J.; Andersen, O. K. Band theory and Mott insulators: Hubbard U instead of Stoner I. *Phys. Rev. B: Condens. Matter Mater. Phys.* **1991**, *44*, 943.

(44) Liechtenstein, A.; Anisimov, V.; Zaanen, J. Density-functional theory and strong interactions: Orbital ordering in Mott-Hubbard insulators. *Phys. Rev. B: Condens. Matter Mater. Phys.* **1995**, *52*, R5467.

(45) Wang, L.; Maxisch, T.; Ceder, G. Oxidation energies of transition metal oxides within the GGA+U framework. *Phys. Rev. B: Condens. Matter Mater. Phys.* **2006**, *73*, 195107.

(46) Kim, J.; Middlemiss, D. S.; Chernova, N. A.; Zhu, B. Y.; Masquelier, C.; Grey, C. P. Linking Local Environments and Hyperfine Shifts: A Combined Experimental and Theoretical ^{31}P and ^{7}Li Solid-State NMR Study of Paramagnetic Fe(III) Phosphates. *J. Am. Chem. Soc.* **2010**, *132*, 16825−16840.

(47) Masquelier, C.; Tabuchi, M.; Ado, K.; Kanno, R.; Kobayashi, Y.; Maki, Y.; Nakamura, O.; Goodenough, J. B. Chemical and Magnetic Characterization of Spinel Materials in the $LiMn_2O_4$ − $Li_2Mn_4O_9$ − $Li_4Mn_5O_{12}$ System. *J. Solid State Chem.* **1996**, *123*, 255−266.

(48) Dovesi, R.; Orlando, R.; Civalleri, B.; Roetti, C.; Saunders, V. R.; Zicovich-Wilson, C. M. CRYSTAL: a computational tool for the ab initio study of the electronic properties of crystals. *Z. Kristallogr. - Cryst. Mater.* **2005**, *220*, 571−573.

(49) Becke, A. D. Density-functional thermochemistry. III. The role of exact exchange. *J. Chem. Phys.* **1993**, *98*, 5648−5652.

(50) Pell, A. J.; Kervern, G.; Emsley, L.; Deschamps, M.; Massiot, D.; Grandinetti, P. J.; Pintacuda, G. Broadband inversion for MAS NMR with single-sideband-selective adiabatic pulses. *J. Chem. Phys.* **2011**, *134*, 024117.

(51) Carlier, D.; Ménétrier, M.; Grey, C. P.; Delmas, C.; Ceder, G. Understanding the NMR shifts in paramagnetic transition metal oxides using density functional theory calculations. *Phys. Rev. B: Condens. Matter Mater. Phys.* **2003**, *67*, 174103.

(52) Bhattacharya, J.; Van der Ven, A. Phase stability and nondilute Li diffusion in spinel $Li_{1+x}Ti_2O_4$. *Phys. Rev. B: Condens. Matter Mater. Phys.* **2010**, *81*, 104304.

(53) Harris, K. J.; Foster, J. M.; Tessaro, M. Z.; Jiang, M.; Yang, X.; Wu, Y.; Protas, B.; Goward, G. R. Structure Solution of Metal-Oxide Li Battery Cathodes from Simulated Annealing and Lithium NMR Spectroscopy. *Chem. Mater.* **2017**, *29*, 5550−5557.